



Cite this: DOI: 10.1039/d2nr00251e

Electronic properties of graphene oxide: nanoroads towards novel applications†

Almaz I. Khabibrakhmanov ^{a,b,c} and Pavel B. Sorokin ^{a,b}

In this work, we suggest an approach to manipulate the electronic properties of graphene oxide in a controllable manner. We study graphene nanoroads paved inside graphene oxide using density functional calculations. We show that this patterning allows transforming an insulator, graphene oxide, into a semiconductor or metal depending on the orientation of the nanoroads and their magnetic state. As a semiconductor, patterned graphene oxide is characterized by notably low effective masses of charge carriers. Additionally, we demonstrate the possibility to force the transition from a semiconducting to a half-metallic state in a controllable manner, by application of an external electric field. We believe that this remarkable opportunity to combine and control the electronic and magnetic properties of a material within a single sheet of graphene oxide paves the way towards new applications of graphene-oxide-based devices in 2D optoelectronics and spintronics.

Received 14th January 2022,
Accepted 23rd January 2022

DOI: 10.1039/d2nr00251e

rsc.li/nanoscale

Introduction

Graphene oxide (GO) is a rising star among two-dimensional materials and has attracted significant attention in the last two decades due to its easily scalable and low-cost synthesis.^{1,2} GO was suggested as a promising material for numerous applications in sensing, energy storage, 2D electronics and optoelectronics, photocatalysis, and memristors.^{2,3} This great tailorability of GO properties is apparently due to a rich variety of possible chemical compositions and structures.

Generally, GO can be imagined as a single graphene sheet functionalized by oxygen-containing chemical groups, and according to the available experimental data the elemental ratio of C:O:H in GO can vary from 6:2.33:1.2 to 6:3.7:2.83 depending on the synthesis method and chemical conditions.⁴ To further extend the practical applications of GO, it is highly important for the whole GO community to sort out the connections between the chemical composition, atomic structure and electronic properties of GO.

The synthesized GO with a high oxidation level is commonly believed to be an insulator with the band gap ~2–4

eV,^{5–8} which limits the potential applicability of GO in electronics. So, numerous researchers attempted to narrow the band gap of GO, mainly by a controlled reduction of as-synthesized GO.^{9–11} However, due to the statistical nature of GO as a material, experiments can give only the average picture of the processes occurring in GO, and a more detailed understanding is often lacking.

At this point, *ab initio* calculations come into play, since they are a powerful tool providing an insightful physical-chemical picture of various effects in materials at the atomic level. At the moment, *ab initio* calculations have proven themselves well in the studies of GO providing useful insights into the atomic structure, thermodynamic stability, and electronic properties of GO.^{12–24} To perform a computational study, it is important to choose the appropriate structural model of GO. Since the GO phase diagram is very rich, it is not surprising that its atomic structure still stays a subject of active dispute.²⁴ Nevertheless, some important structural motifs of GO are already well identified experimentally as well as theoretically and might be considered as commonly accepted.

One of the GO structural models widely used was proposed by Lerf and Klinowski^{25,26} based on NMR measurements. In this model, GO is depicted as randomly distributed flat aromatic (unoxidized) graphene islands separated from each other by oxidized regions with epoxide (–O–) and hydroxyl (–OH) functional groups dominating inside them. Later, extensive experimental research using transmission electron microscopy, X-ray absorption, and Raman spectroscopy techniques confirmed the dominance of epoxide and hydroxyl groups in GO and demonstrated that islands of clear graphene and oxidized regions alternate on a nanometer scale.^{27–30}

^aNational University of Science and Technology MISIS, 4 Leninskiy prospekt, Moscow, 119049, Russian Federation.

E-mail: almaz.khabibrakhmanov@phystech.edu, pbsorokin@misis.ru

^bMoscow Institute of Physics and Technology (National Research University), 9 Institutskiy per., Dolgoprudny, Moscow Region, 141701, Russian Federation

^cDepartment of Physics and Materials Science, University of Luxembourg, L-1511 Luxembourg City, Luxembourg

†Electronic supplementary information (ESI) available: Atomic structures and additional figures providing more details and information about the studied systems. See DOI: 10.1039/d2nr00251e

The tendency of oxygen groups to aggregate on graphene was also reported in the numerous theoretical studies of GO.^{12,13,19,20,23,24,31} In particular, Yan *et al.*^{12,13} found out that the lowest-energy structures of partially oxidized GO are those with graphene ribbons in the unit cell. Recently, Mouhat *et al.*²⁴ directly compared semiordered and random structural models of GO. The random models were created by uniformly distributing oxygen groups over a graphene surface, whereas in the semiordered models oxygen groups were partially clustered together with pristine graphene regions in between forming a kind of nanoroad. Interestingly, semiordered structures were reported to be energetically more favorable.²⁴ Thus, a fully oxidized GO matrix patterned by graphene nanoroads (GONR') may be regarded as a reasonable structural model for the *ab initio* study of GO electronic properties.

The electronic properties of graphene nanoroads paved in graphane and fluorographane (GNR') were studied theoretically by the Yakobson group.^{32,33} It was revealed that GNR' demonstrate a non-trivial dependence of the electronic structure on the nanoroad width and interface type (armchair or zigzag). It is believed that the physical origin of the peculiar electronic properties observed is the quantum confinement of massless Dirac electrons of graphene.^{32,33} However, the experimental creation of such confined graphene structures using hydrogen atoms still remains a big challenge. In contrast, GO is much easier to synthesize compared to graphane or fluorographane. Similar to graphane and fluorographane, GO has a wide band gap, which allows one to expect similar effects of quantum confinement for electrons in nanoroads. These facts suggest that using GO as a host matrix may be a promising approach for practically obtaining graphene nanoroads. Therefore, it is especially interesting to systematically study the electronic properties of GONR'.

Another reason to study GONR' is the resistive switching effect that was experimentally found in GO.^{34–40} Resistive switching means that properly fabricated GO samples can switch between high and low resistance states depending on the external electric field. Although this phenomenon has been studied for a decade already,^{34–40} its detailed mechanism at the atomic level remains largely unknown. Interestingly, one of the proposed mechanisms consists of the formation of conductive graphitic channels in the GO matrix.^{35,36,38,40} So, obtaining knowledge about the electronic properties of various GO compositions under the impact of an electric field may give some insights into the resistive switching mechanism in GO.

Summing up, through this work we would like to show that GO is a prospective two-dimensional material with widely tunable electronic properties, which was not commonly recognized before. We carried out a comprehensive *ab initio* study of how the electronic properties of GO can be modified by paving graphene nanoroads, and we demonstrate that GO can serve as a perfect host matrix for the realization of the peculiar electronic properties of graphene nanoroads. We begin with the study of possible periodic GO structures fully covered by

epoxide and hydroxyl groups and find the most thermodynamically stable phases among them. Furthermore, we consider GONR' with armchair and zigzag orientations paved inside the host matrix of these energetically favorable GO structures. We thoroughly study their thermodynamic, electronic (band gap and effective masses), and magnetic properties. Finally, we investigate how a lateral electric field can affect the electronic structure of GONR' and show the possibility for a smooth switch from a semiconducting to a half-metallic state.

Computational details

All calculations were done in the framework of density functional theory (DFT).^{41,42} Electron exchange–correlation was treated in generalized gradient approximation as proposed by Perdew–Burke–Ernzerhof (GGA-PBE).⁴³ For the case of zigzag GONR', the spin-polarized formalism was utilized.

The calculations of the atomic structure and electronic properties of fully oxidized GO and GONR' were carried out using the projector augmented wave (PAW) method,^{44,45} as implemented in VASP.^{46,47} The plane wave energy cutoff was set equal to 550 eV. Periodic boundary conditions (PBCs) were employed along in-plane lattice vectors of simulation cells, whereas the out-of-plane lattice vector was set as long as 20 Å to prevent unphysical interactions between periodic images. Both lattice vectors length and atomic coordinates were allowed to relax until interatomic forces converged to within 0.01 eV Å^{−1}. The stress tensor components for unit cells were found to be less than 0.5 GPa after the relaxation. The *k*-point sampling of the 2D Brillouin zone was done adopting Γ -centered Monkhorst–Pack grids⁴⁸ with a uniform spacing of $2\pi \times 0.02$ and $2\pi \times 0.01$ Å^{−1} for geometry relaxations and DOS calculations, respectively. Additionally, the energies of pristine graphene, O₂, and H₂ molecules were calculated with the same computational setup to enable the evaluation of fully oxidized GO and GONR' formation enthalpies.

The effect of a lateral electric field on the electronic structure of zigzag GONR' was evaluated using SIESTA code⁴⁹ with the double- ζ plus polarization (DZP) basis set of numerical atomic orbitals.⁵⁰ Core electrons were replaced by norm-conserving Troullier–Martins pseudopotentials⁵¹ in their fully nonlocal representation,⁵² and the real space mesh cutoff was set to be equal to 300 Ry. For this part of our study, 1D ribbons were produced out of 2D periodic supercells of zigzag GONR'. PBCs were retained in the direction along a nanoroad, whereas a vacuum as thick as 20 Å was additionally introduced to a supercell in the direction perpendicular to the ribbon edge. The ribbon edges were passivated by H atoms, and the atomic geometry was reoptimized. The same density of *k*-points and atomic force convergence criteria as above were preserved. The external electric field (ϵ) was simulated through a periodic sawtooth-type potential applied perpendicular to the ribbon edge, with the slab dipole correction to electrostatic potential and energies enabled.⁵³

Results and discussion

Fully oxidized GO

Let us begin with the study of various fully oxidized GO structures. We consider these structures as the host matrices, inside which we then pave graphene nanoroads. Therefore, we found it reasonable to limit ourselves to moderate size periodic unit cells at this stage. In previous theoretical studies,^{12,13,15,19–23} mainly epoxide-rich phases of GO were investigated and several ground-state structures with C_8O_4 stoichiometry were proposed. For hydroxyl-rich GO, existing studies agree on a single energetically most favorable periodic structure with the formula $C_8(OH)_8$.^{12,13,22,23}

To resolve the mentioned ambiguity with the C_8O_4 ground-state atomic structure, we selected the favorable structures reported in the literature and carried out their geometry relaxation to directly compare the total energies. The obtained atomic geometries were found to be in full agreement with those reported in the reference papers.^{12,13,15,19–23} Fig. 1a displays the energetic diagram of the considered C_8O_4 structures. The phases C_8O_4 -i and C_8O_4 -ii were first suggested in the work¹⁹ where C_8O_4 -i was found to be slightly lower in energy, and therefore it attracted some interest also later.^{20,21} In agree-

ment with Šljivančanin *et al.*,¹⁹ we also found that C_8O_4 -i is lower in energy than C_8O_4 -ii though the energy difference is quite small (31 meV per unit cell). The structures labeled as iii, iv, and v in Fig. 1a were reported by Guilhon *et al.*²² with C_8O_4 -iii and C_8O_4 -iv also being considered in earlier studies.^{12–15} The authors²² used the cluster expansion approach along with the DFT-PBE calculations to find all possible symmetry-degenerate periodic phases of fully oxidized GO. C_8O_4 -iii was reported to be the lowest energy phase of C_8O_4 stoichiometry in that work. However, our results show that in fact the structures C_8O_4 -i and -ii have lower energies. This contradiction can be easily explained since the search was constrained by the initial hexagonal shape of the unit cell with 8 atoms,²² whereas C_8O_4 -i and -ii possess an orthorhombic symmetry (see Fig. 1a). This explains why these structures were overlooked in the work²² despite adopting the robust statistical method of cluster expansion.

To understand the relationship between the energy and the structure of C_8O_4 , one should consider the latter in more detail. All five C_8O_4 structures follow a favorable oxidation pattern when the neighboring oxygen atoms are adsorbed from the opposite sides of a graphene sheet. This induces buckling of the carbon backbone in the opposite directions,

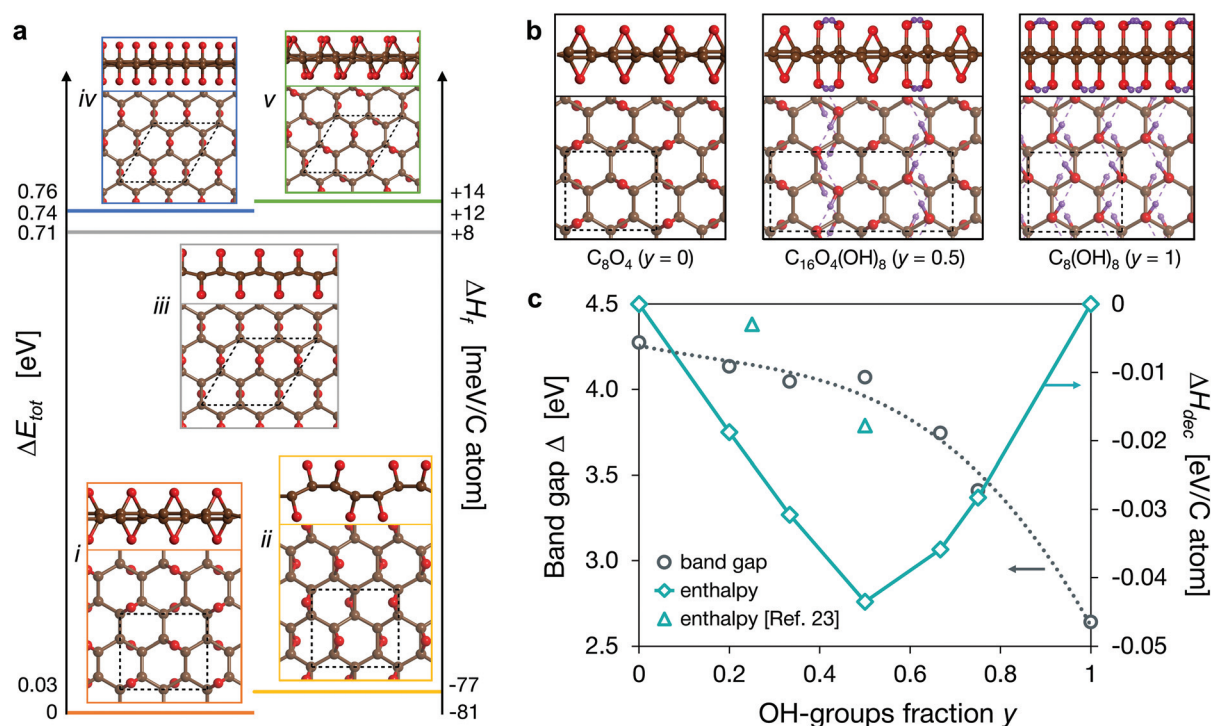


Fig. 1 (a) The energy diagram of the favorable GO phases with C_8O_4 stoichiometry. Side and top views are shown for each phase. The unit cells are marked with black dashed lines. The total energy differences ΔE_{tot} on the left are given with the reference to the lowest energy structure C_8O_4 -i which we call “epoxy-GO”. On the right scale, the calculated formation enthalpies ΔH_f are displayed. (b) The energetically favorable structures of fully oxidized GO with different compositions (left to right): epoxy-GO, mixed GO, and hydroxy-GO. The hydrogen bond network is schematically shown by purple dashed lines. (c) The dependence of band gap (black circles) and decomposition enthalpy ΔH_{dec} (azure diamonds) on the fraction y of OH-groups for the mixed GO phases. For the images of the corresponding atomic structures we refer the reader to Fig. S1 of the ESI.† The triangles display decomposition enthalpy ΔH_{dec} for the two most favorable mixed structures $C_8O_2(OH)_4$ and $C_8O_3(OH)_2$ reported by Guilhon *et al.*²³ Note the different y-axes on the left and right. The cubic polynomial fitting of the band gap dependence is shown with a black dotted line, and the enthalpy data points are connected with solid azure lines to guide the eye.

and strains induced in the graphene lattice by the oxidation are compensated better.^{12,13} The energy differences between C_8O_4 phases should then originate from the arrangement of epoxide groups within one side of the sheet. As it can be seen from Fig. 1a, C_8O_4 -iii, -iv, and -v are very close in energies that can be explained by the similarity of their oxidation patterns. Also, the distances between the two nearest oxygen atoms in them are quite close being 2.59, 2.64, and 2.49 Å, respectively. In contrast, C_8O_4 -i and -ii are significantly (~ 0.7 eV per unit cell) lower in energy due to a more homogeneous and distant arrangement of oxygen atoms. The most optimal pattern is observed in C_8O_4 -i where oxygen atoms form a regular rhombic sublattice with the period of 3.38 Å. The largest spatial separation of neighboring epoxides allows the minimization of the electrostatic repulsion between their electronic clouds and thus the minimization of the total energy. A similar explanation applies also to the stability of $C_8(OH)_8$ that is achieved by the antiparallel arrangement of OH-groups into 1,2-pairs on the hexagonal graphene backbone (see Fig. 1b). 1,2-hydroxyl pairs on both sides of the sheet are lined up along the armchair direction of the graphene lattice. This is due to the presence of hydrogen bonds (showed by a purple dash in Fig. 1b), which additionally stabilize the structure.

To further analyze the thermodynamic stability of fully oxidized GO structures, the formation enthalpy (ΔH_f) of GO (E_{GO}) with respect to pristine graphene C_8 (E_C), O_2 (E_{O_2}) and H_2 (E_{H_2}) molecules was computed *via* the formula:

$$\Delta H_f = \frac{1}{N_C} \left(E_{GO} - \frac{1}{8} N_C E_C - \frac{1}{2} N_O E_{O_2} - \frac{1}{2} N_H E_{H_2} \right), \quad (1)$$

where N_C , N_O , and N_H are the number of carbon, oxygen, and hydrogen atoms in the structure, respectively. The formation enthalpy is normalized per the number of carbon atoms.

The results obtained for C_8O_4 are also shown in Fig. 1a and prove the importance of finding the appropriate ground-state structure. As one can see, only C_8O_4 -i and -ii have negative formation enthalpy, whereas the other structures which were considered stable earlier²² exhibit positive enthalpy and therefore should be thermodynamically unstable relative to graphene and oxygen molecule. As for $C_8(OH)_8$, it possesses negative $\Delta H_f = -1.59$ eV per carbon atom and is highly stable. Thus, for the chosen size of the unit cell, we find C_8O_4 -i and $C_8(OH)_8$ to be the ground-state structures of epoxide- and hydroxyl-rich GO, so we named them as “epoxy-GO” and “hydroxy-GO”, respectively.

To complete the description of fully oxidized GO, we also considered the structures of mixed compositions (*i.e.*, containing both –O– and –OH groups). Such GO models were also the objects of the previous studies.^{12–15,18,23} It is useful to view them as composed of three components: graphene, epoxy- and hydroxy-GO. Within this approach, all possible GO stoichiometries are conveniently represented on a ternary phase diagram, which was shown to be helpful for the thermodynamic analysis in the earlier studies.^{12,13,23} For the case of fully oxidized GO, the ternary phase diagram reduces to a

binary one, with the epoxy- and hydroxy-GO on its ends. To create mixed GO structures, we first used the insights from studies by Yan *et al.*^{12,13} and combined various proportions of epoxy- and hydroxy-GO unit cells within the new mixed cell. We shall recall this as a “cut-and-glue” approach (see $C_{16}O_4(OH)_8$ in Fig. 1b and the other structures in Fig. S1 of the ESI†). As a second option, we included into the analysis the most favorable mixed structures $C_8O_2(OH)_4$ and $C_8O_3(OH)_2$ (Fig. S1†) reported by Guilhon *et al.*²³ Finally, we considered structures where the elementary building blocks C_2O and $C_2(OH)_2$ were randomly placed inside a graphene unit cell comprising 8 carbon atoms (Fig. S1†). We chose $C_2(OH)_2$ as an elementary block rather than $C_1(OH)_1$ since it is well-known from the previous studies of the GO atomic structure^{12,13} that adsorption of an unpaired –OH group is less likely due to the breakage of the conjugated π -electronic system of graphene and appearance of an unpaired π -electron that increases the energy.

Overall, the stoichiometry of the considered mixed GO phases can be represented as $[CO_x(OH)_y]_{8m}$, where m is a natural and $8m = N_C$, $0 \leq x \leq 0.5$ and $0 \leq (y = 1 - 2x) \leq 1$. After the geometry optimizations, we retrieved the total energies E_{mix} and evaluated the enthalpy of decomposition ΔH_{dec} of the mixed GO into pure epoxy-GO (E_{ep}) and hydroxy-GO (E_{hyd}) according to the equation:

$$\Delta H_{dec} = \frac{1}{N_C} (E_{mix} - 2xmE_{ep} - ymE_{hyd}). \quad (2)$$

As in the case of ΔH_f , this enthalpy is normalized per carbon atom. We found that ΔH_{dec} is positive for our randomly created models, *i.e.* thermodynamically they tend to decompose into pure epoxy- and hydroxy-GO. The negative ΔH_{dec} values were found for the cut-and-glue structures and also for $C_8O_2(OH)_4$ and $C_8O_3(OH)_2$ suggested by Guilhon *et al.*,²³ *i.e.* for the structures where the local atomic environment was preserved as in epoxy- and hydroxy-GO. We note that this observation is in agreement with the previous general conclusions^{12,13} made regarding the stability of various GO structures.

The dependence of ΔH_{dec} on the fraction y of –OH groups in mixed GO phases is presented in Fig. 1c. For $C_8O_2(OH)_4$ and $C_8O_3(OH)_2$ (marked by triangles), we obtained ΔH_{dec} equal to –18 and –3 meV per C atom, or –0.142 and –0.024 eV per unit cell, respectively. We remark that our values differ from the ΔH_{dec} values originally reported²³ for $C_8O_2(OH)_4$ (–0.72 eV per unit cell) and $C_8O_3(OH)_2$ (–0.67 eV per unit cell). This is due to the alternative choice of the reference structure in the original paper²³ as C_8O_4 -iii, which is, however, not stable by itself in terms of the formation enthalpy ΔH_f (Fig. 1a). As for the cut-and-glue structures, they are all characterized by the negative decomposition enthalpy with the largest magnitude among the considered mixed GO phases. The lowest value $\Delta H_{dec} = -44$ meV per C atom is achieved for the $C_{16}O_4(OH)_8$ phase shown in Fig. 1b.

Now let us briefly overview the electronic properties of fully oxidized GO. To extract the band gap Δ , we calculated the electronic density of states (DOS) and band structure for the cut-and-glue mixed GO phases, and for epoxy- and hydroxy-GO as

Table 1 The structural parameters, energetics, and band gap values of the three selected fully oxidized GO phases in comparison with those of graphene C_8H_8 . a_{AC} and a_{ZZ} are the orthorhombic lattice constants along the armchair and zigzag directions of the carbon backbone, respectively. The corresponding PBE values for pristine graphene are $a_{AC,gr} = 4.275$ Å and $a_{ZZ,gr} = 4.936$ Å. The formation enthalpy ΔH_f is calculated according to eqn (1). γ_{AC} and γ_{ZZ} are the energies of the armchair and zigzag interfaces between the considered structures and pristine graphene. Values of the band gap Δ obtained in this work are compared to the previous theoretical results.

	a_{AC} , Å	a_{ZZ} , Å	ΔH_f , eV per C atom	γ_{AC} , eV Å ⁻¹	γ_{ZZ} , eV Å ⁻¹	Δ , eV
C_8O_4 -i	4.422	5.113	-0.081	0.09	0.14	4.3 ^a , 3.9 ^b , 4.1 ^c , 6.5 ^d
$C_{16}O_4(OH)_8$	4.474	10.254	-0.878	0.09	0.12	4.1 ^a , 5.0 ^c , 4.1 ^f
$C_8(OH)_8$	4.513	5.310	-1.589	0.02	0.06	2.6 ^a , 2.8 ^f , 4.3 ^g
C_8H_8	4.402	5.081	-0.204	0.14	0.17	3.5 ^a , 3.2 ^h , 3.5 ⁱ

^a This work. ^b PBE. ²⁰ ^c PBE. ²¹ ^d B3LYP. ²¹ ^e PBE. ¹⁵ ^f LDA. ¹² ^g HSE. ¹⁸ ^h PBE. ³² ⁱ PBE. ⁵⁴

well. The dependence of the band gap on the fraction y of -OH groups is shown in black in Fig. 1c. As one can see, the band gap of fully oxidized GO smoothly changes in the wide range from 4.3 eV to 2.6 eV, with these extreme values being determined by the limiting cases of epoxy- and hydroxy-GO. The band gaps calculated in this work and reference papers for epoxy-, hydroxy-, mixed GO and graphene (for comparison) are presented in Table 1 along with the data on their structure and thermodynamics. As one can see, our values of Δ show a good agreement with the previous DFT results and fall well within the range of the reported experimental values. The differences between our calculations and those done using hybrid functionals^{18,21} are due to a well-known systematic underestimation of band gaps within the DFT-PBE approximation. So, the good correspondence of our PBE results for 100% oxidized GO to the experimental band gaps should be rather attributed to the incomplete oxidation of experimental GO samples, since full oxidation is hard to achieve and rarely observed in practice. Nevertheless, we believe that the PBE results allow us making correct qualitative predictions, as it was shown previously.^{15,20,21} The trend in Fig. 1c indicates that the fundamental gap of GO can be widely tuned by controlling its chemical composition. Furthermore, we are going to demonstrate that patterning GO by graphene nanoroads is a way to achieve even more subtle control over the electronic properties of GO.

Atomic structure and energetics of GONR'

We considered graphene nanoroads of various widths paved in fully oxidized GO. To cover the variety of GO compositions, we chose three fully oxidized GO phases that were discussed in the previous section: epoxy-GO and hydroxy-GO as the limiting points on the GO phase diagram, and $C_{16}O_4(OH)_8$ as the mixed GO phase with the lowest decomposition energy ΔH_{dec} (Fig. 1a and b).

Analogous to the studies of graphene and fluorographene,^{32,33} GONR' were designed by removing functional groups from fully oxidized GO to form a pristine graphene nanoroad terminated by armchair (AC) or zigzag (ZZ) interfaces, and the resulting structures are named as $N_{AC}(x)$ -AGONR' or $N_{ZZ}(x)$ -ZGONR', respectively. Here, N_{AC} and N_{ZZ} characterize a nanoroad width and denote the number of graphene dimer lines (Fig. 2a) and zigzag chains (Fig. 3a), accordingly, whereas (x) is the name of the parental fully oxidized GO

phase: "epoxy", "hydroxy", or "mixed". Note that due to the specific arrangement of oxygen groups only nanoroads with even N_{AC} are possible in epoxy-GO, whereas there are no restrictions in all the other cases.

In the study of nanoroads, it is important to ensure that a well-defined and sharp (at the atomic level) GO/graphene interface can be formed. To verify this, we designed perfect GO/graphene interfaces, then removed the functional group from the interface, and calculated the energy penalty for placing the group to the closest adsorption site in the graphene domain (*i.e.* an interfacial defect was introduced). We performed these calculations for increasing unit cell widths to obtain the dependence of the penalty energy on the interfacial defect concentration (Fig. S2†). The obtained ultimate values of penalty energy $E_{pen}(-O-) = 1.5$ eV and $E_{pen}(-OH) = 2.7$ eV for the removal of *isolated* epoxy- and hydroxy-groups from the perfect interface are comparable to the respective value for hydrogen in graphene (2.32 eV).³² This indicates that atomically perfect GO/graphene interfaces should be highly stable since the energy cost for interfacial defect formation cannot be overcome at reasonable temperatures.

Next, we evaluated the perfect GO/graphene interface formation energies γ_{AC} and γ_{ZZ} along the armchair and zigzag directions, respectively. We also included in our analysis nanoroads in graphene to enable a direct comparison. For these calculations, supercells containing wide nanoroads ($N_{AC} > 10$, $N_{ZZ} \geq 6$) and a graphene domain of the same width were generated. The atomic geometries were relaxed as described in the Computational details section, and the total energies were retrieved. Furthermore, we adopted the computational method introduced by Yakobson *et al.*^{55,56} to extract the interface formation energies γ_{AC} and γ_{ZZ} . The results acquired are presented in Table 1. In all cases, we found armchair interfaces to be preferable over zigzag ones by their excess energy. The values of $\gamma_{AC} = 0.14$ eV Å⁻¹ and $\gamma_{ZZ} = 0.17$ eV Å⁻¹ for graphene are in a good agreement with DFTB results by Singh *et al.*⁵⁵ (0.12 and 0.18 eV Å⁻¹, respectively). As for the GO phases, they all appear to form more favorable interfaces than graphene. Hydroxy-GO demonstrates especially low values of both γ_{AC} (0.02 eV Å⁻¹) and γ_{ZZ} (0.06 eV Å⁻¹). Interfaces with epoxy-GO have the highest formation energy among GO phases ($\gamma_{AC} = 0.09$ eV Å⁻¹ and $\gamma_{ZZ} = 0.14$ eV Å⁻¹), whereas mixed GO represents an intermediate case between epoxy- and hydroxy-GO

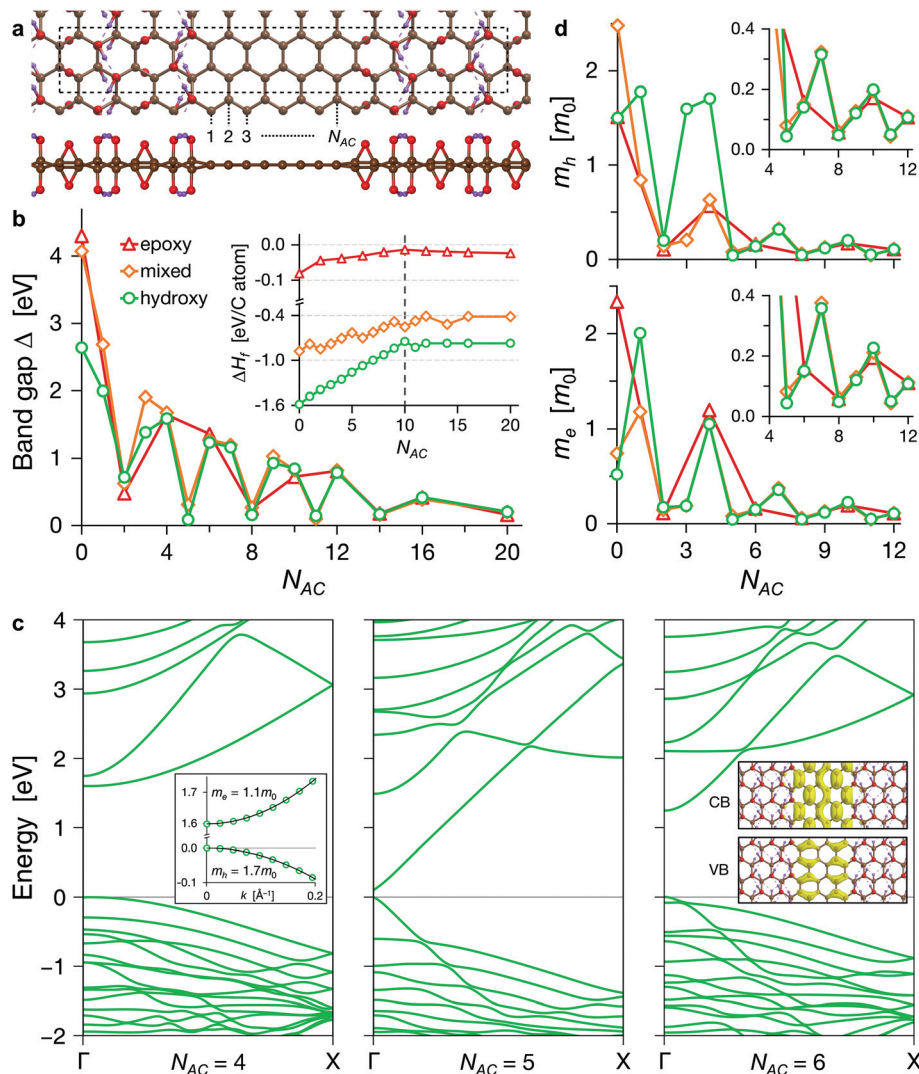


Fig. 2 (a) The atomic structure of 8-mixed-AGONR' (top and side views are given). The dashed box shows the orthorhombic unit cell used in calculations. The numbers (1, 2, 3, ..., N_{AC}) indicate the number of dimer lines constituting the nanoroad width. (b) The dependence of AGONR' band gap Δ on the nanoroad width N_{AC} for the three considered GO compositions: epoxy-GO (red), mixed GO (orange), and hydroxy-GO (green). The inset shows their formation energies ΔH_f calculated via eqn (1). The dashed line denotes a division of the studied structures onto two families with varying ($N_{AC} \leq 10$) and roughly constant ($N_{AC} > 10$) ratios of sp^2 -carbon atoms within the unit cell (see the text). (c) The band structures of 4-, 5-, and 6-hydroxy-AGONR'. The valence band maximum (VBM) was set to zero. The insets illustrate: ($N_{AC} = 4$) calculation of the effective masses; ($N_{AC} = 6$) band-decomposed charge density isosurfaces ($1.5 \times 10^{-3} \text{ e } \text{\AA}^{-3}$) for the top valence band (VB) and the bottom conduction band (CB) of 6-hydroxy-AGONR'. See also Fig. S4† for the other GO compositions. (d) The effective masses of holes (upper panel) and electrons (lower panel) as a function of the AGONR' index. Colors agree with the frame (b), and the insets show the same dependences magnified for the widths $N_{AC} > 4$. All pictures of the atomic structures and charge density distributions in this work are made using the VESTA software,⁵⁷ and the band structures are plotted with the aid of the *pymatgen* library for materials analysis.⁵⁸

($\gamma_{AC} = 0.09 \text{ eV } \text{\AA}^{-1}$ and $\gamma_{ZZ} = 0.12 \text{ eV } \text{\AA}^{-1}$). Overall, these results indicate that perfect GO/graphene interfaces can be formed at relatively low energy costs, and the consideration of the model structure patterned with nanoroads is justified. For more detailed information about the results and calculation methods used in this part of our study, we refer the reader to the ESI (Fig. S3†).

To carry out a systematic study of the electronic properties of GONR', narrower structures were designed for all three GO compositions, with the nanoroad widths N_{AC} and N_{ZZ} taking

all possible values up to 12 and 6, respectively. The examples of the relaxed atomic geometries for AGONR' and ZGONR' are presented in Fig. 2a and Fig. 3a, b. Similar to the cases of graphene and fluorographene, the geometry of all AGONR' remained flat, whereas among zigzag GO nanoroads only hydroxy-ZGONR' manifested a tilt in the graphene domain that was observed for zigzag nanoroads in graphene and fluorographene. The tilt emerges due to the positions of -OH groups at the zigzag edges which cause the opposite buckling directions of the opposite nanoroad sides across the nanoroad (Fig. 3a).

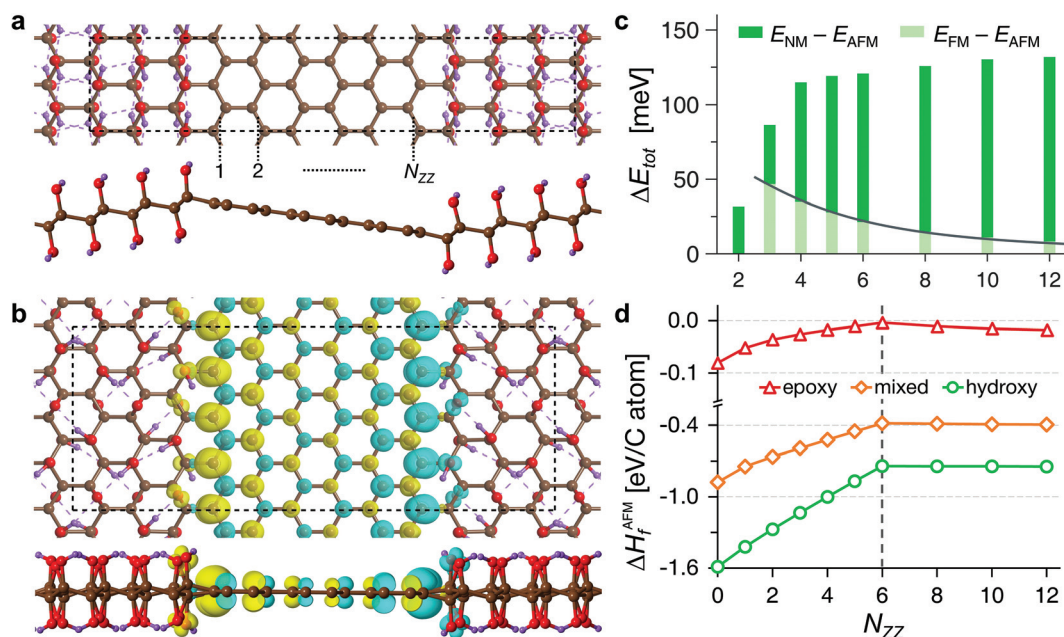


Fig. 3 The atomic structures of (a) 6-hydroxy- and (b) 6-mixed-ZGONR' (top and side views). The dashed boxes denote the orthorhombic unit cells used in calculations. The numbers (1, 2, ..., N_{ZZ}) mark zigzag carbon chains making up a graphene nanoroad. Additionally, in panel (b) the isosurface ($0.01 \text{ e } \text{\AA}^{-3}$) of spin density corresponding to the AFM spin arrangement is shown. Yellow and cyan colors denote α - and β -spin densities, respectively. (c) The differences of total energy ΔE_{tot} (per unit cell) between AFM, FM, and NM spin configurations of hydroxy-ZGONR' as a function of the nanoroad width. The energy differences are calculated relative to the AFM configuration as a ground state. The gray solid line displays the fitting of $E_{\text{FM}} - E_{\text{AFM}}$ energy difference with the inverse square law (see the text). (d) The formation enthalpy ΔH_f of AFM ZGONR' for various nanoroad widths N_{ZZ} . As in the case of AGONR', all studied structures can be divided into two families with varying ($N_{ZZ} \leq 6$) and roughly constant ($N_{ZZ} > 6$) ratios of sp^2 -carbon atoms within the unit cell.

As for epoxy- and mixed-ZGONR', these nanoroads remained flat, despite also having zigzag edges.

This difference with the previous cases can be easily explained, since $-\text{H}$, $-\text{F}$, and $-\text{OH}$ groups are all monovalent and turn sp^2 -hybridized graphene into a sp^3 -hybridized layer with the alternate buckling of two graphene sublattices. This is, however, not the case for epoxy-groups which form covalent bonds with two carbon atoms simultaneously.

As a result, buckling of neighboring atoms is compensated along both AC and ZZ directions in epoxy- and mixed GO (e.g., see 6-mixed-ZGONR' structure in Fig. 3b), and all nanoroads created in these GO phases retain a flat atomic structure.

It is also important to mention that all AGONR' considered in this study exhibit a negative formation energy ΔH_f (see the inset in Fig. 2b). The vertical dashed line in this graph for ΔH_f denotes the division of GONR' considered in this work into two families. The first includes nanoroads with N_{AC} up to 10 which were paved within the supercell of a fixed size. Subsequently, the fraction of sp^2 -carbon atoms in these AGONR' linearly increases together with N_{AC} , and thus ΔH_f as defined by eqn (1) also grows linearly with N_{AC} . In contrast, the remaining AGONR' were designated for the interface energy calculations and therefore had varying supercell sizes but approximately the same ratio ($\sim 50\%$) of the sp^2 -graphene therein. This leads to the roughly constant values ΔH_f as one

can see in the described graph. The same holds for ZGONR' as well, with the only difference in a borderline value of $N_{ZZ} = 6$ (Fig. 3d). Thus, the seeming non-homogeneity of ΔH_f trends for both AGONR' and ZGONR' is not a physical effect but rather emerges due to the diversity of the studied systems. Both AGONR' and ZGONR' studied in this work appear to be thermodynamically stable.

Furthermore, we calculated the electronic density of states and band structure for the considered GONR' structures, including those designed for the calculation of interface energies. Thus, the electronic properties of GO patterned by nanoroads were studied in a wide range of nanoroad widths ($1 \leq N_{\text{AC}} \leq 20$, $1 \leq N_{ZZ} \leq 12$) for the three different chemical compositions. The following two sections provide a detailed description of our results.

Electronic properties of AGONR'

From the band structure analysis, we revealed that all AGONR' are direct band gap (except $N_{\text{AC}} = 1$) semiconductors, independent of the original GO composition. Moreover, AGONR' of the three compositions show very similar oscillating dependence of band gap on N_{AC} (see Fig. 2b). The notable differences can be observed only at small widths due to the differences in band gaps of the parental GO phases (see Table 1) and the significant influence of the interfaces. With increasing N_{AC} , the data points for different GO compositions become closer, and

they are almost identical for the widest nanoroads considered. This fact confirms the common physical nature of the emerging band gaps – quantum confinement, as in graphane and fluorographene.^{32,33}

The band gap behavior can be divided into three hierarchical families for $N_{AC} = 3p$, $3p + 1$, and $3p + 2$, where p is a positive integer. Each family displays an almost monotonous descending trend with increasing width keeping the rule $\Delta_{3p+2} < \Delta_{3p+1} < \Delta_{3p}$ for $p > 1$. This behavior is different from the one found for armchair graphene nanoribbons⁵⁹ but similar to that observed for nanoroads in graphane and fluorographene,^{32,33} or graphene with periodically adsorbed hydrogen chains.^{60–62}

The typical band structures of hydroxy-AGONR' are presented in Fig. 2c (see Fig. S4 of ESI† for epoxy- and mixed AGONR'). As shown in the inset, the charge densities corresponding to the top valence band (VB) and the bottom conduction band (CB) are mostly confined in a graphene domain with a small leakage to the GO matrix, which indicates the dominating role of graphene nanoroads in the charge carriers' transport. We also would like to draw attention to the fact that both VB and CB manifest well-pronounced dispersion. Since the curvature of bands is directly related to effective masses of charge carriers in semiconductors, one might expect the effective masses to be quite low in AGONR'. To quantify our observation, we calculated the effective masses of electrons (m_e) and holes (m_h) in AGONR'. We used the textbook definition:

$$m^* = \hbar^2 \left(\frac{\partial^2 E}{\partial k^2} \right)^{-1} \quad (3)$$

and performed the parabolic fitting for the top VB and the bottom CB in the vicinity of their extrema (see the inset in Fig. 2c). The obtained results are presented in Fig. 2d. For both electrons and holes, the effective masses obey the rule $m_{3p+2} < m_{3p} < m_{3p+1}$ (for $p > 1$) displaying a monotonous decay in magnitude with increasing p . It is also appealing that starting from $N_{AC} = 5$ effective masses m_e and m_h become identical and both oscillate in the range $0.04\text{--}0.38m_0$ (m_0 is the free electron mass). These masses are comparable (or even less) than those in ordinary semiconductors like Si and Ge,⁶³ and very similar to those in armchair graphene nanoribbons ($0.05\text{--}0.17m_0$,⁶⁴ $0.07\text{--}0.22m_0$).⁶⁵ In the limit of infinite graphene, the effective masses tend to zero as they should. In general, our results in this section demonstrate how patterning GO by armchair nanoroads allows combining the properties of an insulator and a semiconductor with low effective masses within a single atomic sheet.

Electronic and magnetic properties of ZGONR'

It is well known that zigzag edges of graphene are characterized by the localized low-energy π -states,^{66,67} and these states were also observed experimentally by scanning tunneling microscopy techniques.^{68,69} It was realized that zigzag edge states can give rise to edge magnetism in graphene ribbons,^{66,67} in graphene nanoroads^{32,33} and in graphene with

periodically adsorbed hydrogen chains.⁶² Therefore, the electronic properties of ZGONR' should be studied taking into account the possible magnetic arrangements of zigzag edge states. We considered three magnetic configurations: non-magnetic (NM, was obtained in non-spin-polarized calculations), ferromagnetic (FM), and antiferromagnetic (AFM). The latter two terms refer to the parallel or antiparallel (see Fig. 3b) orientation of magnetic moments located on two graphene sublattices of a nanoroad, respectively. We revealed that only the NM configuration exists for the narrowest 1-ZGONR', whereas for $N_{ZZ} > 1$ the AFM arrangement is the one with the lowest energy. The FM configuration was found to emerge starting from $N_{ZZ} = 3$, and it is intermediate in energy between AFM and NM states.

We found that the exact chemical composition of GO does not influence this energetic hierarchy of ZGONR' magnetic states, leading just to somewhat scattered values of energy differences for them (see Fig. 3c and Fig. S5 of the ESI†). The energy difference $E_{NM} - E_{AFM}$ saturates at $N_{ZZ} = 6$ to the values $\sim 100\text{--}130$ meV per unit cell‡ that agrees very well with ~ 110 meV reported by Singh and Yakobson³² for nanoroads in graphane. The difference $E_{FM} - E_{AFM}$ is even smaller (Fig. 3c) and it rapidly decreases from $\sim 30\text{--}50$ meV per unit cell for 3-ZGONR' to $7\text{--}8$ meV per unit cell for 12-ZGONR' (that is, being comparable to the error of the computations). This decrease can be fitted with the inverse square law $A/(N_{ZZ}^2 + B)$, where $A \sim 1.2 \times 10^3$ and $B \sim 15\text{--}30$ depending on the GO composition (see the gray solid lines in Fig. 3c and Fig. S5†). The scaling $E_{FM} - E_{AFM} \propto w^2$ arises due to the superexchange inter-edge coupling present between the spin states from the opposite sides of a nanoroad.⁷⁰ Similar trends in energy differences $E_{FM} - E_{AFM}$ and $E_{NM} - E_{AFM}$ were also reported for graphene nanoribbons.⁷¹

The found energetic ordering AFM-FM-NM is in full agreement with that established for graphene nanoribbons with widths up to $N_{ZZ} = 32$.⁷² Moreover, our findings on magnetic ZGONR' in GO are consistent with the previous results for ZGNR' in graphane and fluorographene^{32,33} and show very similar trends. The increasing energy difference between non-magnetic and magnetic phases (Fig. 3c and Fig. S5†) indicates that the magnetism should be maintained also in wider nanoroads.

Antiferromagnetic ZGONR' are semiconductors with spin-degenerate bands (Fig. 4a and Fig. S6,† left panels), whereas all ferromagnetic ZGONR' are found to be metallic in both spin channels (Fig. 4a and Fig. S6,† right panels). The width dependence of the antiferromagnetic ZGONR' band gap is shown in Fig. 4b. Mostly, the behavior of the band gap is very similar for all three GO compositions. Starting from $N_{ZZ} \geq 4$ it falls off via the inverse law $\Delta = A/(N_{ZZ} + B)$ from $0.4\text{--}0.5$ to $0.2\text{--}0.3$ eV, very similar to the cases of GNR⁵⁹ and nanoroads

‡ Note that mixed-ZGONR' structures have their unit cells twice bigger than epoxy- and hydroxy-ZGONR' due to the different periodicity of the parental mixed GO structure $C_{16}O_4(OH)_8$ in a zigzag direction. Therefore, for the case of mixed GO the calculated energy differences are additionally divided by two to enable a direct comparison.

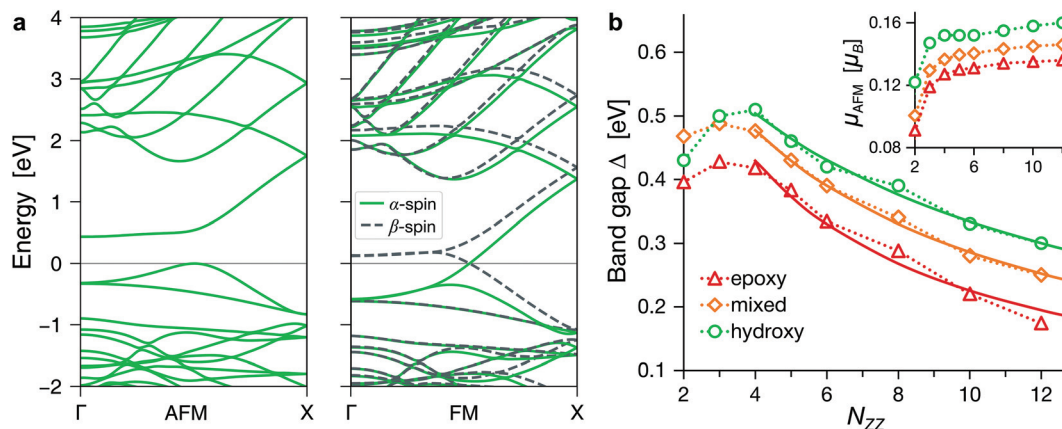


Fig. 4 (a) Typical band structures of the AFM (left) and FM (right) configurations at the example of 6-hydroxy-ZGONR'. In the case of AFM, all bands are spin-degenerate. VBM is set to energy zero. Band structures for the other compositions can be found in Fig. S6.† (b) The dependence of anti-ferromagnetic ZGONR' band gap Δ on the nanoroad width N_{ZZ} . The fitting (starting from $N_{ZZ} = 4$) with the hyperbolic law is shown with solid lines of the corresponding colors. Here, A and B are the constants different for each composition. In the inset, local magnetic moments μ_{AFM} (in μ_B per atom) projected onto the outermost atoms of ZZ nanoroads with AFM spin arrangement (see Fig. 3b) are plotted against N_{ZZ} . The dotted lines are to guide an eye. For the analogous dependence in the case of FM spin arrangement please see Fig. S8.†

in fluorographene.³³ Deviation from this law for smaller widths can be attributed to stronger quantum confinement and interface effects. This is proven also by the dependence of local magnetic moments on the outermost atoms of nanoroads (see the inset in Fig. 4b). In addition, we estimated the effective masses of charge carriers for antiferromagnetic epoxy-ZGONR', as it was done for AGONR' above. We found that there is a significant difference between the masses of electrons and holes. Namely, m_e increases with broadening a nanoroad and reaches $3.2\text{--}3.5m_0$ for $N_{ZZ} > 4$, whereas m_h decreases from $0.27m_0$ to $0.13m_0$ in the range of $N_{ZZ} = 4\text{--}12$ (see Fig. S7 of the ESI†).

Apparently, magnetic states on the two opposite edges of a nanoroad become spatially separated enough only for $N_{ZZ} > 4$, which is expressed in a further saturation of the local magnetic moment. The same is also true for the ferromagnetic ZGONR' (Fig. S8†) and for ferromagnetic GNR.⁷¹ There is also a correlation between the values of the magnetic moment and band gap for different GO compositions. Namely, the ZGONR' with a larger magnetic moment has a wider band gap at a given nanoroad width (Fig. 4b). The fact that the magnetic moment and band gap are influenced by the GO composition throughout the whole range of nanoroad widths can be explained if we consider the spin density distribution. The spin density is mainly localized near the nanoroad interfaces (see Fig. 3b) and exponentially decays to its center,⁷² therefore even in relatively wide nanoroads the magnetic moment and band gap remain sensitive to the GO matrix composition. This is in notable contrast with the case of AGONR' (Fig. 2b), where the charge density is delocalized over a nanoroad and the distinctions in band gap between different GO compositions vanish when increasing the nanoroad width (due to a diminishing contribution from the interfaces).

Here we should also note the earlier study of GO thermoelectric properties by Zhou *et al.*⁷³ where the electronic pro-

perties of GONR' were explored to some extent as well. However, this was not the main focus of the work,⁷³ and the consideration therein was limited to two GO models, both of them containing epoxide groups alone. One of them (type I⁷³) corresponds to our C_8O_4 -iii phase that is not the ground-state for GO of the C_8O_4 composition, as we showed above. We additionally considered the second model (type II⁷³) which appeared to be even less favorable with the formation enthalpy of $\Delta H_f = +43$ meV per C atom. This choice of the parental GO phases for patterning by nanoroads explains why the formation enthalpies of GONR' reported⁷³ are always positive in contrast to our results (see the inset in Fig. 2b and Fig. 3d).

Despite this fact, we would like to note a remarkable agreement in the band gap *vs.* N_{AC} obtained for AGONR' in our work and the reference⁷³ (see Fig. 2b of both manuscripts). However, there are some differences in the case of ZGONR' (*cf.* Fig. 4b with Fig. 2b⁷³). For type I ZGONR', Zhou *et al.*⁷³ predicted much larger band gaps than what we found, and on the contrary, almost vanishing band gaps (below 0.1 eV for $N_{ZZ} > 2$) were calculated for type II ZGONR'. We think these discrepancies are due to the disregard of spin polarization in the discussed work⁷³, which is crucially important when it comes to the determination of the ground state of ZGONR'.

Nevertheless, the results obtained by Zhou *et al.*⁷³ represent the study of non-magnetic ZGONR' configurations, and therefore they may be considered as complementing the present study that is mainly focused on AFM and FM arrangements. In the next section we investigate how the lateral electric field might influence the electronic properties of AFM ZGONR'.

Electric-field-induced half-metallicity of ZGONR'

The antiferromagnetic arrangement of zigzag edge states in ZGONR' enables manipulating the electronic structure by applying the electric field ϵ across a nanoroad. This idea was first suggested by Son *et al.*⁷² who showed that in such a way

zigzag graphene nanoribbons can be turned into a half-metal. Here we show that a similar effect can also be observed for ZGONR'. As described in the Computational details section, the ribbons for this part of our study were formed out of 6-, 8- and 10-ZGONR' structures of all three GO compositions, having equal widths of graphene and GO regions (see Fig. 5a). Dangling bonds on the ribbon edges were passivated by hydrogen atoms. The so-obtained ribbons were reoptimized with the sufficient vacuum space provided in two directions.

We switched to the SIESTA code for this type of calculation, since the localized basis set of atomic orbitals is expected to suit better the simulations where localized electronic states are subjected to the external electric field, comparing to the plane-wave basis set. Another, more practical reason to switch to SIESTA is due to a notably higher computational cost of plane-wave calculations for simulation cells with a large vacuum space which we have to use here. We note that in all previous studies of this effect in graphene nanoribbons^{72,74,75} *ab initio* codes with the localized basis sets were employed as well. To provide consistency with the previous parts of our study, in our SIESTA calculations we used the same theoretical approximations and, when possible, the same numerical algorithms and convergence criteria, as we employed before in VASP. An excellent agreement between the two codes was obtained that is proven by the comparison of calculated atomic and band structures of the same ZGONR' (Fig. S9†).

With this said, let us turn to the discussion of our results for considered ribbons with the embedded ZGONR'. The example of the atomic structure together with spin density dis-

tribution is shown in Fig. 5a. Except for the small distortion due to the absence of PBCs in the transverse direction and hydrogen passivation of the edges, the atomic structure of the ribbons remained almost the same as that of the respective ZGONR'. The same holds also for their band structure in zero electric fields (see Fig. S9†).

With the transverse electric field applied, the band gap for the electrons with β -spin narrows, whereas the gap for the opposite spin electrons widens (Fig. 5b). Therefore, there should be a critical value of the electric field when the gap for β -spin electrons vanishes, *i.e.* it becomes metallic. Since α -spin electrons only increase their energy gap, this means that the system makes a transition from a semiconducting to a half-metallic state. The gap for β -spin electrons is closed indirectly, resulting in both electron and hole channels at E_F (see the inset in the right panel of Fig. 5b). For 10-epoxy-ZGONR' the transition occurs at $\varepsilon = 0.2 \text{ V \AA}^{-1}$, two β -spin bands cross the Fermi level, and the nanoribbon becomes half-metallic.

The physical explanation of the effect is due to the localized edge states in ZGONR'. The electric field leads to the shifts of the electrostatic potentials in the opposite directions for the left and right edges of ZGONR'. Since the opposite spin states are localized on the opposite sides of ZGONR', the electric field ε pushes β -spin states towards each other, whereas the α -spin states are pulled apart (see the scheme in Fig. 5c). We would like to note that our findings are consistent with the original work by Son *et al.*⁷² on the analogous effect in GNR.

Since it is the difference of the electrostatic potential between the left and right sides of ZGONR' which determines

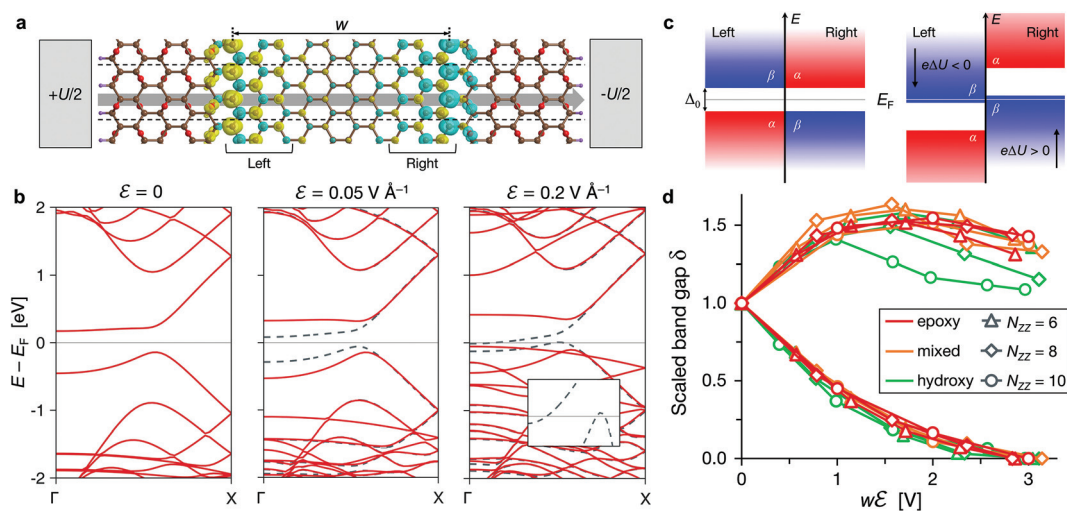


Fig. 5 (a) Ribbon formed out of 10-epoxy-ZGONR' in the transverse electric field (the direction is indicated by a gray arrow). The ribbon is periodic in the direction orthogonal to the field, the unit cell boundaries are shown with black dashed lines. Antiferromagnetic spin density distribution (0.01 e \AA^{-3} isosurface) in the ground state, without the external field, is also displayed. Yellow and cyan colors denote α - and β -spin densities, respectively. (b) Band structure of the ribbon from panel (a) in the varying electric field (left to right): $\varepsilon = 0$, 0.05 , and 0.2 V \AA^{-1} . The Fermi energy (E_F) is set to zero. Red solid and black dashed lines denote the bands with α - and β -spins, respectively. The inset in the right frame shows the magnified behavior of bands in the vicinity of E_F (horizontal line). (c) The schematic illustration of the spin-resolved local DOS of the AFM ribbon without the external field (left frame) and with the applied transverse electric field (right frame). "Left" and "right" in the picture refer to the opposite sides of the nanoroad embedded in the ribbon, as indicated in panel (a). (d) Scaled band gaps for α - and β -spin electrons as a function of $w\varepsilon$ for the three nanoroad widths: $N_{ZZ} = 6$ (triangles), 8 (diamonds), 10 (circles). α - and β -spins are not distinguished explicitly by colors but this should not lead to ambiguity, since always $\delta_\beta \leq 1$ and $\delta_\alpha \geq 1$. See Fig. S10† for the same data presented separately for each GO composition.

the energy shifts for electrons, the critical electric field required for half-metallic transition is expected to decrease with the widening of ZGONR'. Our results for ZGONR' of a fixed GO composition and varying width verify this consideration showing a monotonous decrease of critical ε values (Fig. S10†), in coherence with the findings for GNR.^{72,74} The key role of the electrostatic potential difference in the effect can be additionally confirmed, if we consider the scaled band gaps for two spins defined as $\delta_{\alpha,\beta} = \Delta_{\alpha,\beta}(w,\varepsilon)/\Delta_0(w)$, where $\Delta_{\alpha,\beta}(w,\varepsilon)$ is the band gap for $\alpha(\beta)$ -spins of the ZGONR' with a width w in external field ε , and $\Delta_0(w) = \Delta_{\alpha}(w,\varepsilon = 0) = \Delta_{\beta}(w,\varepsilon = 0)$. The dependence of dimensionless $\delta_{\alpha,\beta}$ on the product $w\varepsilon$, *i.e.* on the voltage drop, is shown in Fig. 5d. We emphasize that despite different nanoroad widths and compositions, δ_{α} and especially δ_{β} show the universal behavior that can be described by a single function of $w\varepsilon$, as in the case of graphene nanoribbons.⁷² This fact again evidences that the electronic properties of ZGONR' are weakly influenced by the exact chemical composition of the parental GO, which is the important result of our work. Discrepancies observed in Fig. 5d for the α -spin gap of mixed and hydroxy-GO are attributed just to the changed order of valence bands when compared to epoxy-GO. Contribution to the VBM state in mixed and hydroxy-GO becomes dominated by oxygen atoms, whereas in the case of epoxy-GO this oxygen-dominated band lies lower in energy and therefore both CBM and VBM come from carbon-dominated bands (see Fig. S11† for the detailed explanation). Anyway, this affects only the α -spin gap and therefore does not change our conclusion about the universal character of the half-metallic transition in ZGONR'. We found the threshold value of $w\varepsilon$ to be in the range 2.85–3.15 V depending on the GO composition and nanoroad width which gives 3.0 V on average. This can be compared to 3.0 V obtained for graphene nanoribbons using DFT-LDA calculations.⁷²

Finally, we find it important to mention that our results may shed some light on the mechanism of resistive switching that is well-known to take place in GO.^{34–40} One of the most common hypotheses is that when the electric field of a certain strength is applied to GO (so-called “forming voltage”), the conducting graphene filaments are formed in the originally insulating GO matrix due to the surface migration of oxygen groups. Then, the so-formed GO can demonstrate the switching between high and low resistance states at the operating voltages that can be already significantly lower than the forming voltage. This switching is also thought to be achieved by the migration of oxygen groups which in this case interrupts the conducting graphene channels. We believe that GO patterned by graphene nanoroads might also serve as a model structure for GO in the formed state. As demonstrated by this work, the formed nanoroads manifest various band gaps depending on their width, and even a subtle change of a nanoroad (*e.g.* due to the oxygen group migration) can drastically change its electronic properties, which may result in the observed resistive switching behavior. We also showed here that the external electric field can influence electronic properties as well, at least for zigzag nanoroads. We suppose that all these effects might con-

tribute to the complex mechanism of resistive switching, and once nm-scale GO nanoroads are synthesized, this hypothesis might be checked experimentally.

Conclusions

In this manuscript, we presented the results of our complex computational study of graphene oxide as a material with widely tunable structure and electronic properties. Using density functional calculations, we considered various phases of fully oxidized GO and determined the most favorable structures among them. For the three selected stoichiometries, armchair and zigzag graphene nanoroads were paved in GO, and their thermodynamic, electronic, and magnetic properties were thoroughly studied for a broad range of nanoroad widths.

We showed that graphene nanoroads form highly stable, low-energy interfaces with GO and demonstrate the non-trivial dependence of electronic properties on a nanoroad width. Armchair nanoroads are characterized by the oscillating decrease of the band gap when widening a nanoroad, and the same trend was observed for the charge carriers' effective masses with their lowest values being in the range 0.05–0.2 m_e for wide enough nanoroads that sounds promising for applications of patterned GO as a 2D semiconductor. Our results provide a possible explanation for the wide range of GO band gaps observed experimentally.

The electronic properties of zigzag nanoroads were found to be intimately connected to their magnetic state. Non-magnetic and ferromagnetic states are metastable and lead to a metallic conductivity, whereas an antiferromagnetic arrangement was found to be a semiconducting ground state for zigzag nanoroads. We have also demonstrated that AFM zigzag nanoroads can change their conductivity from a semiconducting to a half-metallic type when subjected to an external electric field.

All mentioned effects are manifested very similarly for all three GO stoichiometries, which allows us to conclude that the electronic properties of GONR' are mainly determined by graphene regions and weakly depend on the exact chemical composition of the GO matrix. In principle, this should relieve experimentalists from the need to thoroughly control the composition of the synthesized patterned GO without losing its remarkable electronic properties. Together with its cheapness and wide availability, this means that GO could finally become a material where graphene nanoroads with their exciting electronic properties can be observed and measured experimentally.

We believe that the fabrication of the structures patterned by nanoroads of nm width is something that is already possible nowadays. This is by no means an easy task; however, patterning nanoroads is already not just a theoretical concept as well. For example, it was demonstrated already in 2009⁷⁶ that graphene nanoroads can be patterned on hydrogenated graphene. The authors reported the width of the patterned regions to be below 20 nm (5 nm for the narrowest) that was

achieved by the electron-stimulated hydrogen desorption with an STM tip. It is also worth mentioning that the authors noticed drastic changes in the electronic properties caused by the graphene patterning.⁷⁶

Another good example is a recent experimental work,⁷⁷ where the authors managed to manipulate an ensemble of hydrogen atoms with sub-nanometer precision to create graphene nanopatterns. They used STM for this, and the narrowest nanoroads obtained had a width of just 2 nm. Moreover, in the further experiments the authors managed to observe the quantum confinement of electrons in graphene.⁷⁷

Apart from STM, it is also possible to create nanoroads by electron irradiation, as it was shown *e.g.* for fluorinated graphene.⁷⁸ In that work, the authors managed to achieve a decrease of 7 orders of magnitude in resistivity of the electron-irradiated samples, although the obtained nanoroads were relatively wide (40 nm at least). Combining this approach with patterned masks may also allow researchers to study smaller widths.

Finally, we would like to mention dip-pen nanolithography methods, which are rapidly evolving nowadays.⁷⁹ This is a powerful technique allowing nanostructures such as nanowires or nanoribbons to be fabricated with a precise control over their size and shape. For example, dip-pen nanolithography was successfully used earlier to produce graphene nanoribbons.⁸⁰

Summing it up, we believe that using state-of-the-art experimental techniques, such as STM, electron beam irradiation and nanolithography, it should be possible to create graphene nanoroads. Although currently there is no direct evidence for graphene oxide, we believe that these methods successfully applied to hydrogenated and fluorinated graphene can be generalized to the case of oxygen groups as well. We assume that our theoretical predictions may serve as a good motivation for experimentalists to go in this direction, since the possibility to transform GO into a semiconducting structure demonstrated in our work has great potential for practical applications.

By this work, we also hope to attract the researchers focusing on the electronic and transport properties of 2D materials to study GO, which was not widely considered before by their community as a prospective semiconducting material. We hope that our results would be useful for people working in the GO community and beyond.

Conflicts of interest

There are no conflicts to declare.

Acknowledgements

This work was supported by an RFBR grant #19-29-03050. P. B. S. also acknowledges the financial support from the Ministry of Education and Science of the Russian Federation in the framework of the Increase Competitiveness Program of NUST MISIS (K2-2020-023). The calculations were performed at the supercomputer cluster provided by the

Materials Modeling and Development Laboratory at NUST "MISIS" and the Joint Supercomputer Center of the Russian Academy of Sciences. The authors also thank the staff of the Information Technology Department of the Moscow Institute of Physics and Technology and express their gratitude to the Data Center Group for their help in making calculations.

Notes and references

- 1 D. R. Dreyer, S. Park, C. W. Bielawski and R. S. Ruoff, *Chem. Soc. Rev.*, 2010, **39**, 228–240.
- 2 *Graphene Oxide: Fundamentals and Applications*, ed. A. M. Dimiev and S. Eigler, John Wiley & Sons, Ltd, Chichester, UK, 2016.
- 3 F. Li, X. Jiang, J. Zhao and S. Zhang, *Nano Energy*, 2015, **16**, 488–515.
- 4 A. Buchsteiner, A. Lerf and J. Pieper, *J. Phys. Chem. B*, 2006, **110**, 22328–22338.
- 5 K. A. Mkhoyan, A. W. Contryman, J. Silcox, D. A. Stewart, G. Eda, C. Mattevi, S. Miller and M. Chhowalla, *Nano Lett.*, 2009, **9**, 1058–1063.
- 6 T.-F. Yeh, J.-M. Syu, C. Cheng, T.-H. Chang and H. Teng, *Adv. Funct. Mater.*, 2010, **20**, 2255–2262.
- 7 L. Wang, H.-Y. Wang, Y. Wang, S.-J. Zhu, Y.-L. Zhang, J.-H. Zhang, Q.-D. Chen, W. Han, H.-L. Xu, B. Yang and H.-B. Sun, *Adv. Mater.*, 2013, **25**, 6539–6545.
- 8 V. Gupta, N. Sharma, U. Singh, M. Arif and A. Singh, *Optik*, 2017, **143**, 115–124.
- 9 A. Mathkar, D. Tozier, P. Cox, P. Ong, C. Galande, K. Balakrishnan, A. Leela Mohana Reddy and P. M. Ajayan, *J. Phys. Chem. Lett.*, 2012, **3**, 986–991.
- 10 Y. Shen, S. Yang, P. Zhou, Q. Sun, P. Wang, L. Wan, J. Li, L. Chen, X. Wang, S. Ding and D. W. Zhang, *Carbon*, 2013, **62**, 157–164.
- 11 Y. Jin, Y. Zheng, S. G. Podkolzin and W. Lee, *J. Mater. Chem. C*, 2020, **8**, 4885–4894.
- 12 J.-A. Yan, L. Xian and M. Y. Chou, *Phys. Rev. Lett.*, 2009, **103**, 086802.
- 13 J.-A. Yan and M. Y. Chou, *Phys. Rev. B: Condens. Matter Mater. Phys.*, 2010, **82**, 125403.
- 14 L. Wang, Y. Y. Sun, K. Lee, D. West, Z. F. Chen, J. J. Zhao and S. B. Zhang, *Phys. Rev. B: Condens. Matter Mater. Phys.*, 2010, **82**, 161406.
- 15 P. Johari and V. B. Shenoy, *ACS Nano*, 2011, **5**, 7640–7647.
- 16 M.-T. Nguyen, R. Erni and D. Passerone, *Phys. Rev. B: Condens. Matter Mater. Phys.*, 2012, **86**, 115406.
- 17 H. Huang, Z. Li, J. She and W. Wang, *J. Appl. Phys.*, 2012, **111**, 054317.
- 18 X. Jiang, J. Nisar, B. Pathak, J. Zhao and R. Ahuja, *J. Catal.*, 2013, **299**, 204–209.
- 19 Ž. Šljivančanin, A. S. Milošević, Z. S. Popović and F. R. Vukajlović, *Carbon*, 2013, **54**, 482–488.
- 20 F. Nasehnia and M. Seifi, *J. Appl. Phys.*, 2015, **118**, 014304.
- 21 M. Lundie, Ž. Šljivančanin and S. Tomić, *J. Mater. Chem. C*, 2015, **3**, 7632–7641.

- 22 I. Guilhon, F. Bechstedt, S. Botti, M. Marques and L. K. Teles, *Phys. Rev. B*, 2017, **95**, 245427.
- 23 I. Guilhon, F. Bechstedt, S. Botti, M. Marques and L. K. Teles, *J. Phys. Chem. C*, 2017, **121**, 27603–27611.
- 24 F. Mouhat, F.-X. Coudert and M.-L. Bocquet, *Nat. Commun.*, 2020, **11**, 1566.
- 25 H. He, J. Klinowski, M. Forster and A. Lerf, *Chem. Phys. Lett.*, 1998, **287**, 53–56.
- 26 A. Lerf, H. He, M. Forster and J. Klinowski, *J. Phys. Chem. B*, 1998, **102**, 4477–4482.
- 27 D. Yang, A. Velamakanni, G. Bozoklu, S. Park, M. Stoller, R. D. Piner, S. Stankovich, I. Jung, D. A. Field, C. A. Ventrice and R. S. Ruoff, *Carbon*, 2009, **47**, 145–152.
- 28 K. Erickson, R. Erni, Z. Lee, N. Alem, W. Gannett and A. Zettl, *Adv. Mater.*, 2010, **22**, 4467–4472.
- 29 C. Gómez-Navarro, J. C. Meyer, R. S. Sundaram, A. Chuvilin, S. Kurasch, M. Burghard, K. Kern and U. Kaiser, *Nano Lett.*, 2010, **10**, 1144–1148.
- 30 D. Pacilé, J. C. Meyer, A. Fraile Rodríguez, M. Papagno, C. Gómez-Navarro, R. S. Sundaram, M. Burghard, K. Kern, C. Carbone and U. Kaiser, *Carbon*, 2011, **49**, 966–972.
- 31 N. Ghaderi and M. Peressi, *J. Phys. Chem. C*, 2010, **114**, 21625–21630.
- 32 A. K. Singh and B. I. Yakobson, *Nano Lett.*, 2009, **9**, 1540–1543.
- 33 M. A. Ribas, A. K. Singh, P. B. Sorokin and B. I. Yakobson, *Nano Res.*, 2011, **4**, 143–152.
- 34 C. L. He, F. Zhuge, X. F. Zhou, M. Li, G. C. Zhou, Y. W. Liu, J. Z. Wang, B. Chen, W. J. Su, Z. P. Liu, Y. H. Wu, P. Cui and R.-W. Li, *Appl. Phys. Lett.*, 2009, **95**, 232101.
- 35 H. Y. Jeong, J. Y. Kim, J. W. Kim, J. O. Hwang, J.-E. Kim, J. Y. Lee, T. H. Yoon, B. J. Cho, S. O. Kim, R. S. Ruoff and S.-Y. Choi, *Nano Lett.*, 2010, **10**, 4381–4386.
- 36 G. N. Panin, O. O. Kapitanova, S. W. Lee, A. N. Baranov and T. W. Kang, *Jpn. J. Appl. Phys.*, 2011, **50**, 070110.
- 37 O. O. Kapitanova, G. N. Panin, A. N. Baranov and T. W. Kang, *J. Korean Phys. Soc.*, 2012, **60**, 1789–1793.
- 38 S. K. Kim, J. Y. Kim, B. C. Jang, M. S. Cho, S.-Y. Choi, J. Y. Lee and H. Y. Jeong, *Adv. Funct. Mater.*, 2016, **26**, 7406–7414.
- 39 F. Hui, E. Grustan-Gutierrez, S. Long, Q. Liu, A. K. Ott, A. C. Ferrari and M. Lanza, *Adv. Electron. Mater.*, 2017, **3**, 1600195.
- 40 S. Kim, H. J. Jung, J. C. Kim, K.-S. Lee, S. S. Park, V. P. Dravid, K. He and H. Y. Jeong, *ACS Nano*, 2018, **12**, 7335–7342.
- 41 P. Hohenberg and W. Kohn, *Phys. Rev.*, 1964, **136**, B864–B871.
- 42 W. Kohn and L. J. Sham, *Phys. Rev.*, 1965, **140**, A1133–A1138.
- 43 J. P. Perdew, K. Burke and M. Ernzerhof, *Phys. Rev. Lett.*, 1996, **77**, 3865–3868.
- 44 P. E. Blöchl, *Phys. Rev. B: Condens. Matter Mater. Phys.*, 1994, **50**, 17953–17979.
- 45 G. Kresse and D. Joubert, *Phys. Rev. B: Condens. Matter Mater. Phys.*, 1999, **59**, 1758–1775.
- 46 G. Kresse and J. Furthmüller, *Phys. Rev. B: Condens. Matter Mater. Phys.*, 1996, **54**, 11169–11186.
- 47 G. Kresse and J. Furthmüller, *Comput. Mater. Sci.*, 1996, **6**, 15–50.
- 48 H. J. Monkhorst and J. D. Pack, *Phys. Rev. B: Condens. Matter Mater. Phys.*, 1976, **13**, 5188–5192.
- 49 J. M. Soler, E. Artacho, J. D. Gale, A. García, J. Junquera, P. Ordejón and D. Sánchez-Portal, *J. Phys.: Condens. Matter*, 2002, **14**, 2745–2779.
- 50 J. Junquera, Ó. Paz, D. Sánchez-Portal and E. Artacho, *Phys. Rev. B: Condens. Matter Mater. Phys.*, 2001, **64**, 235111.
- 51 N. Troullier and J. L. Martins, *Phys. Rev. B: Condens. Matter Mater. Phys.*, 1991, **43**, 1993–2006.
- 52 L. Kleinman and D. M. Bylander, *Phys. Rev. Lett.*, 1982, **48**, 1425–1428.
- 53 G. Makov and M. C. Payne, *Phys. Rev. B: Condens. Matter Mater. Phys.*, 1995, **51**, 4014–4022.
- 54 J. O. Sofo, A. S. Chaudhari and G. D. Barber, *Phys. Rev. B: Condens. Matter Mater. Phys.*, 2007, **75**, 153401.
- 55 A. K. Singh, E. S. Penev and B. I. Yakobson, *ACS Nano*, 2010, **4**, 3510–3514.
- 56 S. Bhowmick, A. K. Singh and B. I. Yakobson, *J. Phys. Chem. C*, 2011, **115**, 9889–9893.
- 57 K. Momma and F. Izumi, *J. Appl. Crystallogr.*, 2011, **44**, 1272–1276.
- 58 S. P. Ong, W. D. Richards, A. Jain, G. Hautier, M. Kocher, S. Cholia, D. Gunter, V. L. Chevrier, K. A. Persson and G. Ceder, *Comput. Mater. Sci.*, 2013, **68**, 314–319.
- 59 Y.-W. Son, M. L. Cohen and S. G. Louie, *Phys. Rev. Lett.*, 2006, **97**, 216803.
- 60 L. A. Chernozatonskii, P. B. Sorokin and J. W. Brüning, *Appl. Phys. Lett.*, 2007, **91**, 183103.
- 61 L. A. Chernozatonskii, P. B. Sorokin, E. É. Belova, J. Brüning and A. S. Fedorov, *JETP Lett.*, 2007, **85**, 77–81.
- 62 L. A. Chernozatonskii and P. B. Sorokin, *J. Phys. Chem. C*, 2010, **114**, 3225–3229.
- 63 C. Kittel, *Introduction to Solid State Physics*, Wiley, Hoboken, NJ, 8th edn, 2004.
- 64 G. Wang, *Phys. Chem. Chem. Phys.*, 2011, **13**, 11939.
- 65 G. Wang, *Chem. Phys. Lett.*, 2012, **533**, 74–77.
- 66 M. Fujita, K. Wakabayashi, K. Nakada and K. Kusakabe, *J. Phys. Soc. Jpn.*, 1996, **65**, 1920–1923.
- 67 K. Nakada, M. Fujita, G. Dresselhaus and M. S. Dresselhaus, *Phys. Rev. B: Condens. Matter Mater. Phys.*, 1996, **54**, 17954–17961.
- 68 Y. Kobayashi, K. Fukui, T. Enoki, K. Kusakabe and Y. Kaburagi, *Phys. Rev. B: Condens. Matter Mater. Phys.*, 2005, **71**, 193406.
- 69 Y. Niimi, T. Matsui, H. Kambara, K. Tagami, M. Tsukada and H. Fukuyama, *Phys. Rev. B: Condens. Matter Mater. Phys.*, 2006, **73**, 085421.
- 70 J. Jung, T. Pereg-Barnea and A. H. MacDonald, *Phys. Rev. Lett.*, 2009, **102**, 227205.
- 71 L. Pisani, J. A. Chan, B. Montanari and N. M. Harrison, *Phys. Rev. B: Condens. Matter Mater. Phys.*, 2007, **75**, 064418.

- 72 Y.-W. Son, M. L. Cohen and S. G. Louie, *Nature*, 2006, **444**, 347–349.
- 73 S. Zhou, Y. Guo and J. Zhao, *Phys. Chem. Chem. Phys.*, 2016, **18**, 10607–10615.
- 74 E.-J. Kan, Z. Li, J. Yang and J. G. Hou, *Appl. Phys. Lett.*, 2007, **91**, 243116.
- 75 O. Hod, V. Barone, J. E. Peralta and G. E. Scuseria, *Nano Lett.*, 2007, **7**, 2295–2299.
- 76 P. Sessi, J. R. Guest, M. Bode and N. P. Guisinger, *Nano Lett.*, 2009, **9**, 4343–4347.
- 77 E. Cortés-del Río, P. Mallet, H. González-Herrero, J. L. Lado, J. Fernández-Rossier, J. M. Gómez-Rodríguez, J. Veuillen and I. Brihuega, *Adv. Mater.*, 2020, **32**, 2001119.
- 78 F. Withers, T. H. Bointon, M. Dubois, S. Russo and M. F. Craciun, *Nano Lett.*, 2011, **11**, 3912–3916.
- 79 G. Liu, S. H. Petrosko, Z. Zheng and C. A. Mirkin, *Chem. Rev.*, 2020, **120**, 6009–6047.
- 80 Y.-S. Shin, J. Y. Son, M.-H. Jo, Y.-H. Shin and H. M. Jang, *J. Am. Chem. Soc.*, 2011, **133**, 5623–5625.